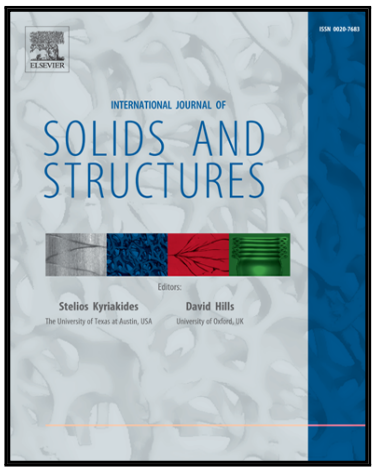

Experimental and Finite Element Analysis of cellular materials under large compaction levels

Bertrand Langrand, Folco Casadei, Vincent Marcadon,
Gérald Portemont, Serge Kruch

PII: S0020-7683(17)30375-X
DOI: 10.1016/j.ijsolstr.2017.08.019
Reference: SAS 9698

To appear in: *International Journal of Solids and Structures*

Received date: 25 April 2016
Revised date: 9 May 2017
Accepted date: 17 August 2017

Please cite this article as: Bertrand Langrand, Folco Casadei, Vincent Marcadon, Gérald Portemont, Serge Kruch, Experimental and Finite Element Analysis of cellular materials under large compaction levels, *International Journal of Solids and Structures* (2017), doi: 10.1016/j.ijsolstr.2017.08.019

Experimental and Finite Element Analysis of cellular materials under large compaction levels

Bertrand Langrand[a,1,*], Folco Casadei[b,2], Vincent Marcadon[a,3], Gérald Portemont[a,1], Serge Kruch[a,3]

[a] *Onera – The French Aerospace Lab*
[b] *European Commission – Joint Research Center*

Abstract

This work aims at investigating the experimental characterisation and the modelling of the mechanical behaviour of cellular sandwich structures for large compaction levels, especially focusing on the collapse mechanisms of their constitutive cells and the role of the contacts created between neighbour cells. For that purpose, brazed cellular sandwich structures made of tube stackings have been considered as model architectures. The experimental characterisation of stackings consisting of either a square pattern or a hexagonal one has highlighted that the collapse mechanism was very reproducible in the case of the square stacking. On the contrary, the one observed for the hexagonal stacking showed an important sensitivity to the architectural defects such as missing braze joints or tube misalignment. Internal self-contacts created played also an important role regarding the densification plateau. In parallel, these compression tests have been simulated through the finite-element method; two different codes have been considered, one implicit (*Z-set*) and one explicit (*Europlexus*). The predictions of both

*Corresponding author: Tel.: +33 3 20 49 69 00; Fax: +33 3 20 49 69 55
Email addresses: bertrand.langrand@onera.fr (Bertrand Langrand), casadeifolco@gmail.com (Folco Casadei), vincent.marcadon@onera.fr (Vincent Marcadon), gerald.portemont@onera.fr (Gérald Portemont), serge.kruch@onera.fr (Serge Kruch)
[1]Materials and Structures Department, F-59014 Lille Cedex France
[2]Retired from European Laboratory for Structural Assessment Unit, I-21027 Ispra (VA) Italy
[3]Materials and Structures Department, F-92322 Châtillon Cedex France

codes have been compared to investigate their differences depending on finite strain and contact formulations. The comparison of their predictions with the experimental results has highlighted that quadratic meshes were necessary, involving the implementation of a second-order pinball method for the modelling of contacts in *Europlexus*. Both codes have also shown very close predictions whatever the mesh order and the finite strain formulation.

Keywords: Cellular material, Mechanical characterisation, Contact algorithm, Finite Element Analysis, Finite strain

---

Nomenclature

ν	Local Poisson ratio
Σ_0	Macroscopic yield stress of the cellular structure
σ_0	Local initial yield stress
Σ_e	Macroscopic collapse stress of the cellular structure
Σ_{22}	Macroscopic nominal stress in the loading direction
$\underline{n}_i$	Normal of pinball i associated surface
$\underline{v}_i$	Velocity of pinball i
$\underline{x}$	Global coordinates
ξ	Normalised coordinates
C	Local isotropic hardening modulus
C_i	Centre position of pinball i
E	Local isotropic elastic modulus
E_e	Macroscopic collapse strain (before consolidation) of the cellular structure
E_{22}	Macroscopic nominal strain in the loading direction
E_{ef}	Effective modulus of the cellular structure

F	Global load
H_0	Initial height of the structure
N	Shape functions
n	Local isotropic hardening exponent
R_i	Radius of pinball i
S_0	Initial cross section of the structure
U_2	Global displacement in the loading direction
W_c	Energy dissipated during the collapse of the cellular structure
W_c^1	Normalized W_c
W_t	Total energy dissipated in the deformation process of the cellular structure

1. Introduction

Cellular materials are widely studied for their various functionalities (Evans et al., 1998) which make them attractive for numerous applications. From a mechanical point of view, higher specific properties are expected with cellular materials compared to the bulk and a large plastic plateau is often observed in compression being very useful in the development of lightweight aeronautical frames in which impact resistance is required for instance. However, the modelling of such cellular materials under large compaction levels presents some difficulties because of the collapse mechanisms observed which involve many contacts, instabilities and large deformations.

In the literature one can find many contributions addressing the characterisation of the elasticity and the beginning of plasticity of such cellular structures, especially regarding the influence of both their architecture and constitutive material properties on their effective behaviour. Without being exhaustive, the reader can refer to the works of Silva and co-authors (Silva and Gibson, 1997; Silva et al., 1995), Fazekas et al. (2002), Sanders and Gibson (2003a,b), Alkhader and Vural (2009) and Marcadon and Kruch (2013) concerning the effect of the morphological parameters or those of Amsterdam et al. (2008a,b), Mangipudi and Onck (2011), Marcadon and Feyel (2009) and Marcadon and Kruch (2011) investigating the effect of the constitutive material behaviour. The issues of large compaction levels and collapse mechanisms are more complex. Experimentally, various architectures have

been characterised under quasi-static loads by Hönig and Stronge (2002), Blazy et al. (2004), Friedl et al. (2008), Marcadon et al. (2012) and under dynamic loads by Hayes et al. (2004) and Papka and Kyriakides (1999a). Especially, very rich results have been obtained addressing the characterisation of the collapse of the constitutive cells, and its influence on the densification plateau (i.e. the domain resulting from the competition between the hardening of the constitutive material and the saturation of the flow stress due to the heterogeneous collapse of the constitutive cells), thanks to the use of X-ray tomography (Burteau et al., 2012; Dillard et al., 2006; Fallet et al., 2008; Jang et al., 2008; Lhuissier et al., 2009).

However, the modelling of the densification plateau and of the final consolidation stage presents some difficulties. Depending on the geometry of the cells, authors proposed different models such as beams in finite strains for Kyriakides and co-authors (Gaitanaros et al., 2012; Jang et al., 2010; Papka and Kyriakides, 1998, 1999b), shell models of real geometries coming from tomography analyses for Caty et al. (2008), or solid models in 2D or 3D for Marcadon and Feyel (2009) and Marcadon et al. (2012). Karagiozova et al. (2006, 2007) proposed an analytical model, based on the geometrical analysis of the hollow sphere collapse, to appreciate the densification plateau generally observed experimentally during the compaction of cellular materials. Shim and Stronge (1986) and Papka and Kyriakides (1998) were pioneers in investigating instability modes in tube stackings under lateral compression. Shim and Stronge (1986) had proposed an analytical model for the compression of tube stacking in the case of confined compression tests on stacked tubes in contact only. Papka and Kyriakides (1998) have focussed on hexagonal stacked tubes made of polycarbonate, a material strongly sensitive to rate effects. The tubes were bounded to each other to form the stacking and the experiments were unconfined. Asymmetrical modes were observed in particular when the cellular structure had geometrical defects. These asymmetrical modes have a negative influence on the mechanical strength of the structures. Symmetrical modes were always observed for perfectly stacked cellular structures (containing no visible, insignificant, defect). Papka and Kyriakides (1998) have also studied the influence of the loading rate, especially because the local displacement rate varied when instabilities progressed in the structures. Instability modes have also been investigated in details by Gong and co-authors (Gong and Kyriakides, 2005; Gong et al., 2005a,b) in the case of open-cell foams. In order to get macroscopic mechanical responses, authors used homogenisation techniques too for non-periodic media, see for

instance the work of Ostoja-Starzewski (2006). Beam elements were also considered in advanced models in order to better capture the architecture and the local collapse mechanisms (Florence and Sab, 2006; Harders et al., 2005; Mangipudi and Onck, 2011; Papka and Kyriakides, 1998). The main drawback of these kind of modelling is the representation of the joints between the tubes which are often considered as rigid bodies. Moreover, many of these models assume a perfectly plastic behaviour for the constitutive material neglecting the contribution of the constitutive material hardening (Fiedler and Öchsner, 2008; Fiedler et al., 2010; Karagiozova et al., 2006, 2007; Sanders and Gibson, 2003a,b).

To address the issue of the modelling of cellular structures under large compaction levels, in the present work cellular structures made of tube stackings have been considered as model architectures because of the reproducibility of both the geometrical and mechanical properties of the tubes. Furthermore, such extruded architectures can be modelled conveniently in 2D. The choice of these particular architectures explains why our literature review has been focused on metal foams, hollow-sphere structures and honeycombs loaded transversally which exhibit similar collapse modes. Section 2 is devoted to the compression tests campaign that has been carried out. After a brief recall of the processing of the samples, the experimental results of the compression tests are discussed regarding the stacking type, e.g. square or hexagonal. Sections 3 and 4 are dedicated to the finite-element modelling of the aforementioned tests using two different finite-element (FE) codes: one implicit *Z-set* and one explicit *Europlexus* (€PX). The cellular structures have been subjected to quasi-static compressive loading conditions. In future works that are not reported here, these cellular structures will be tested under compressive impact loads. There was therefore an interest to compare the numerical results obtained in quasi-static loading conditions from the different computational methods implemented in implicit static code *Z-set* and explicit fast-transient dynamic code €PX. Section 3 focuses on the implementation of a second-order pinball method to improve the modelling of contacts in €PX, whereas Section 4 addresses the modelling assumptions and the various formulations evaluated in terms of mesh elements and finite strain decomposition. A benchmark is proposed in Section 4 between both finite-element codes used to discuss the assumptions of the proposed models. To finish, the predictions of the modelling are also compared with the experimental results to discuss their relevance in Section 5.

2. Experimental analysis

This section addresses the characterisation of the mechanical behaviour of cellular structures under quasi-static load. The structures made of a tube stacking core have been considered as model cellular structures. First the manufacturing process of the cellular structures is briefly described. Then the experimental results obtained by performing compression tests on small sandwich structures are detailed.

2.1. Manufacturing process of the specimens

The cellular materials of interest are brazed tube stackings. The tubes are made of Inconel® 600 alloy which is a standard nickel-base super-alloy used when resistance to corrosion at high temperatures is required. The tubes implemented in the cellular structures have external and internal diameters equal to 5 mm and 4 mm respectively. Skins 1 mm thick, made of the same Inconel® material used for the tubes, were brazed on the top and the bottom faces of the specimens in order to ensure a better distribution of the compressive load.

To manufacture the cellular structures, the tubes were preliminary coated with a 50 μm thickness Nickel-Phosphorus (NiP) alloy layer for the brazing. The NiP layer was needed to create a large joint between the neighbour tubes. The heat treatment considered here consisted in a progressive heating under vacuum at 100°C/mn until 1000°C then followed by a dwell of 15 mn at 1000°C. A complementary annealing heat treatment was applied to make the braze joints less brittle by increasing the diffusion of Phosphorus from the brazes towards the tubes (Davoine et al., 2014). This annealing treatment consisted in a progressive heating under vacuum at 100°C/mn until 1050°C then followed by a dwell of 16 hours at 1050°C. After both heat treatments, the samples were cooled down following the natural cooling of the vacuum furnace. The tubes and the skins were brazed at the same time.

Samples of 40 mm width, 40 mm length and about 42 mm height were manufactured with square or hexagonal stacking cores (Fig. 1). Whereas the structures were 8-tube large for both the square and the hexagonal stacking cores, they were 8-tube high and 9-tube high, respectively. The mean length of the braze joints was about 1.5 mm. The equivalent densities of the cellular structures were 2.69 10^{-3} g.mm^{-3} and 2.89 10^{-3} g.mm^{-3} for the square and hexagonal stacking cores, respectively, making the use of these

materials very attractive compared to the bulk material ($8.25\,10^{-3}\,\mathrm{g.mm^{-3}}$). Before testing, each specimen was at first labelled, measured (height, width and length) and manually inspected to check for possible initial defects (e.g. tube misalignment, missing braze joints).

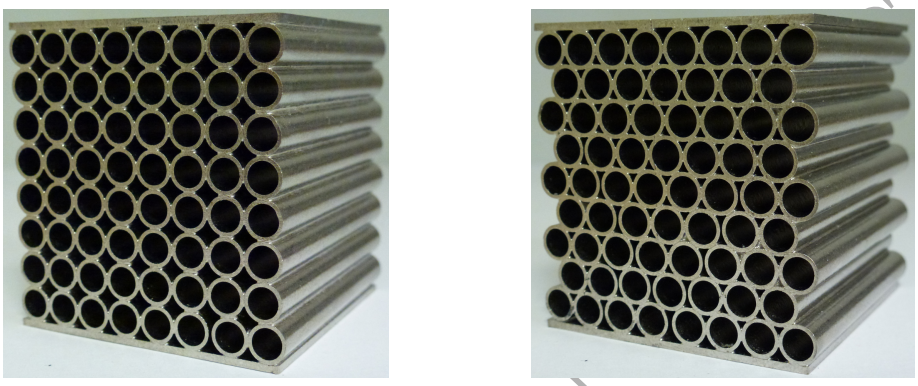

(a) (b)

Figure 1: Cellular structures. (a) square stacking core (b) hexagonal stacking core. The nominal width and length were 40 mm whatever the stacking core. The nominal height was 42 mm and 41.6 mm for the square and hexagonal stacking cores respectively.

2.2. Experimental set-up

The compression tests were performed on an Instron testing machine (ref. 5887) with a load capacity of about 300 kN. The specimens were placed on a fixed circular plate (lower holder) and they were loaded using a plate fixed at the end of the jack (upper holder). A spherical link was used between the jack and the plate. The spherical link made it possible to reduce the influence of the manufacturing defects (e.g. misalignment, specimen flatness) that could affect the mechanical response in particular at the beginning of the test.

The global load, noted F, was measured using a piezoelectric cell (Kistler 9071A) with a load capacity of 400 kN. The load cell was fixed under the lower holder in Fig. 2. The deformation applied to the structure in the loading direction was obtained by the relative distance between the two plates, noted U_2, and was measured with an optical extensometer Zimmer (200XH). Concentricity of the load cell was ensured with the centre of the specimen and that of both plates. A digital camera (Photron, SAX) was used to catch

pictures of the structures during the test. The spacial resolution of the sensor was 1024×1024 pixels. Fig. 2 shows the experimental set-up used to test the structures under compressive load.

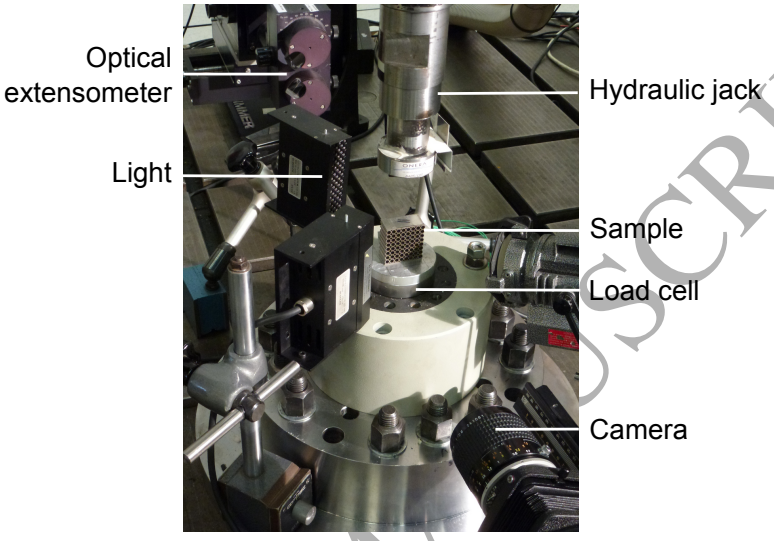

Figure 2: Experimental device.

2.3. Experimental results

The results of the compression tests are presented in terms of nominal stress - nominal strain diagrams. The nominal stress is noted Σ_{22} and is given by $\Sigma_{22} = F/S_0$, with S_0 the initial cross section of the structure (width $\times$ length). The nominal strain is noted E_{22} and is given by $E_{22} = U_2/H_0$, with H_0 the initial height of the structure. Results are presented for both stacking cores investigated for the cellular structures.

2.3.1. Square stacking core

Four (nominally identical) cellular structures with a square stacking core were tested with the experimental device presented in the previous section. Fig. 3 displays the deformation process of the square stacking structure. The linear region was very limited and ended when the tubes located in the center of the core started to collapse (Fig. 3(b)). Other tubes then collapsed to make a first X-shape shear band (Fig. 3(c)). This deformation process could

develop because the specimen was unconfined (lateral faces of the specimen were free). When a X-shear band was formed (tubes were closed) then another one initiated until the densification and the consolidation of the core (Fig. 3(d)).

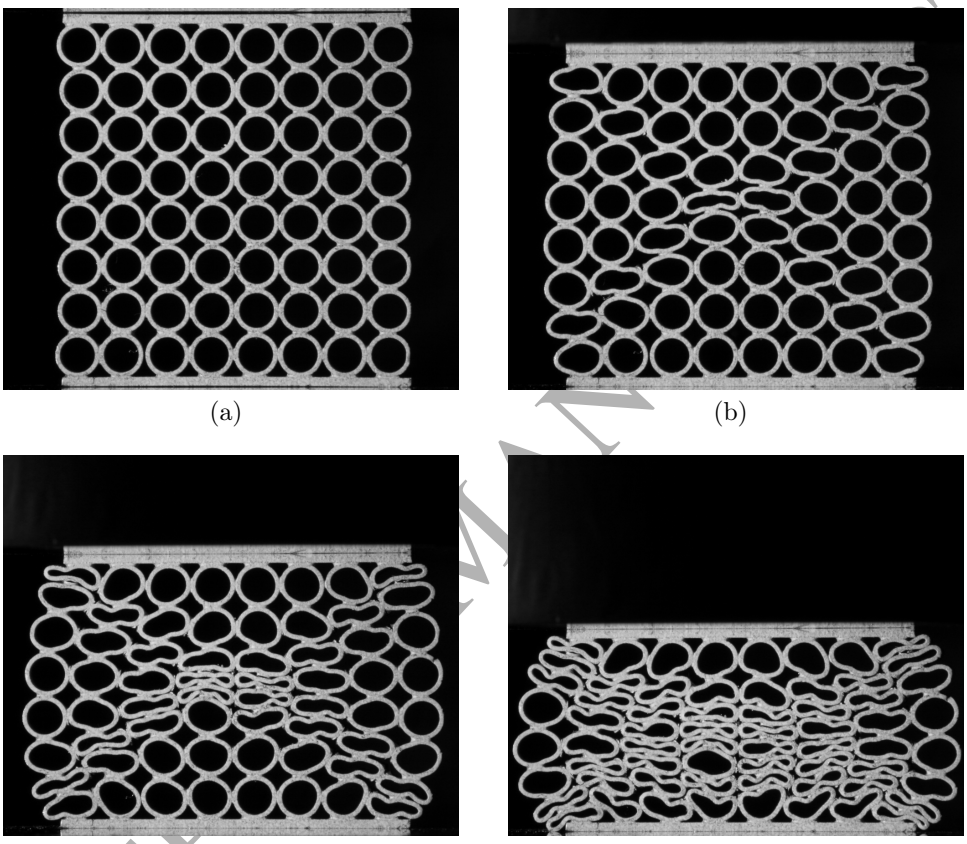

Figure 3: Deformation of the square stacking core cellular structure. (a) $E_{22} = 0$ (b) $E_{22} = -0.10$ (c) $E_{22} = -0.25$ (d) $E_{22} = -0.45$.

The obtained nominal stress - nominal strain response is typical of the behaviour of cellular materials under compressive loads. The nominal stress - nominal strain diagram is very similar whatever the cellular structure used to perform the test (Fig. 4). The linear region is characterised by the effective modulus of the structure (E_{ef}), the plateau corresponding to the collapse

and densification region, characterised by the collapse stress (Σ_c) and a final consolidation region. The collapse strain (before the consolidation of the structure occurred) is noted E_c. The total energy is noted W_t and the collapse energy is noted W_c. The linear region ends at a yield stress noted Σ_0. Due to the collapse of the tubes the yield stress can be greater than the collapse stress.

Mechanical properties are collected in Table 1. The nominal stress - nominal strain curve being flat during the plateau phenomena, the collapse stress was very close to the yield stress. The experimental scattering was slight for most of the mechanical properties analysed from the compression tests, except for the results obtained with specimen C12 that were below other results.

The average effective modulus of the structure was $E_{ef} = 1950\,\text{MPa}$. The collapse of the cellular structure (first tube to collapse) initiated at an almost uniform stress Σ_0 and continued until nominal strains close to -0.22, when the first X-shape shear band was completely formed. The compression nominal stress increased because a second X-shape shear band developed across the core. X-shape shear bands development within the core was a very stable deformation process. The energy absorption was consequently very important during the collapse process. The collapse stress (the average nominal stress) was analysed for nominal strains ranging from the corresponding value of Σ_0 up to the first X-shape shear band was formed (about -0.22). The nominal stress increased significantly at a nominal strain, E_c, of about -0.35, when many X-shape shear bands had completely developed, because of the core consolidation.

Table 1: Mechanical properties of the cellular structure with the square stacking core.

Test number	E_{ef} MPa	$-\Sigma_0$ MPa	$-\Sigma_c$ MPa	$-E_c$.	W_c MPa	$-E_t$.	W_t MPa
C10	2436	19.1	18.8	0.347	6.82	0.456	9.92
C11	2080	17.8	18.1	0.348	6.64	0.457	9.65
C12	1454	15.9	16.2	0.363	6.20	0.455	8.33
C14	1824	19.0	19.3	0.346	6.92	0.463	10.3
average	1948.5	17.9	18.1	0.351	6.64	0.457	9.55

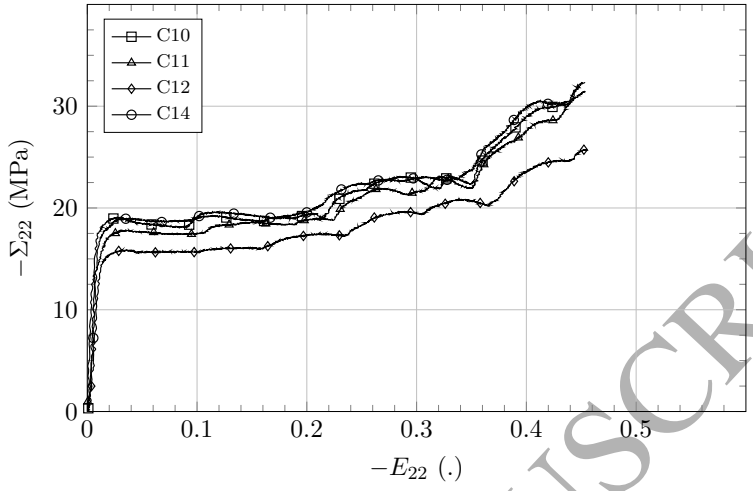

Figure 4: Nominal stress - nominal strain diagrams obtained for the square stacking core.

Some defects were unfortunately present in the cellular specimens due to the manufacturing process. Fig. 5 displays two kinds of initial defects observed for the square stacking core structures. The lowest curve in Fig. 4 was obtained for the structure with missing braze joints between the top skin and the tubes (specimen C12 in Fig. 5(a)). This brazing defect caused an horizontal displacement larger than that observed with the structure without defect. Nevertheless, the force-displacement response was not much affected by tube misalignment and/or when braze joints were missing between tubes.

2.3.2. Hexagonal stacking core

Four (nominally identical) cellular structures with an hexagonal stacking core were tested with the experimental device presented in the previous section. Fig. 6 displays the deformation process of the hexagonal stacking structure. The linear region was very limited and ended when the tubes brazed on the skins started to collapse (Fig. 6(b)). The deformation process of the tubes was very different if brazes were missing between the tubes and the skin (e.g. the top and the bottom skin on Fig. 6(b)). The tubes within the core collapsed until the consolidation of the structure (Fig. 6(d)). The tests were stopped when the consolidation of the structure started (to avoid exceeding the load capacity limits of the experimental set-up).

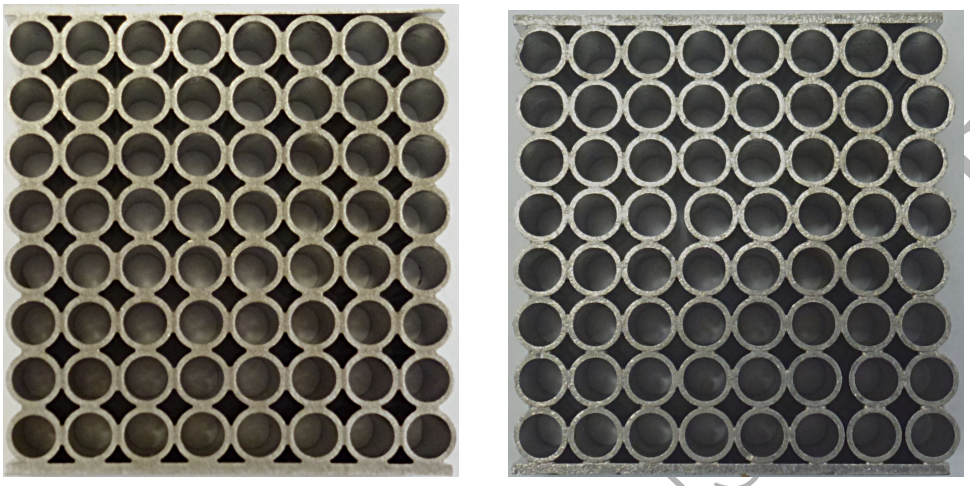

(a) (b)

Figure 5: Initial manufacturing defects in the square stacking core (a) brazes are missing between the top skin and tubes for the specimen of test C12. (b) tubes are misaligned and brazes are missing between tubes for the specimen of test C14.

The analysis of the pictures of the structures taken during each test showed that the core deformations initiated near the brazing defects (Fig. 7). Once the deformation pattern initiated near a defect, a shear band propagated within the core. The different deformation modes were responsible for an irregular/chaotic nominal stress - nominal strain response during the deformation process of the structure (Fig. 8).

Mechanical properties are synthesised in Table 2. The experimental scattering was slight for the yield stress. Because the tests were stopped when the consolidation of the structures had started, the collapse stress (Σ_c) was analysed for nominal strain E_{22} between the corresponding value of Σ_0 until the end of the test. One should notice that the collapse energy was consequently equalled to the total energy. The scattering was slight too for the collapse stress even if the nominal stress - nominal strain response was irregular. The same conclusion stands for the energy.

2.3.3. Stacking influence

Shim and Stronge (1986) have performed confined compression tests and a V-shape shear band collapse mode was observed whatever the stacking

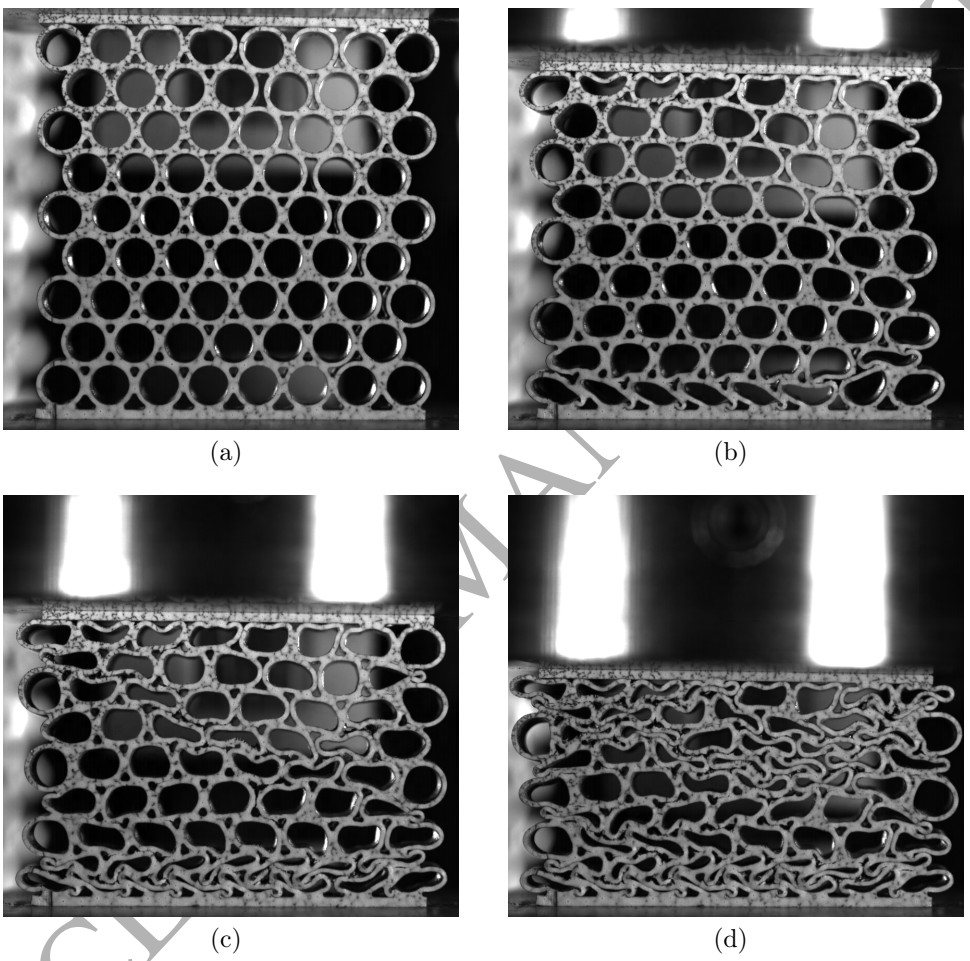

Figure 6: Deformation of the hexagonal stacking core cellular structure H11. (a) $E_{22} = 0$ (b) $E_{22} = -0.12$ (c) $E_{22} = -0.27$ (d) $E_{22} = -0.42$.

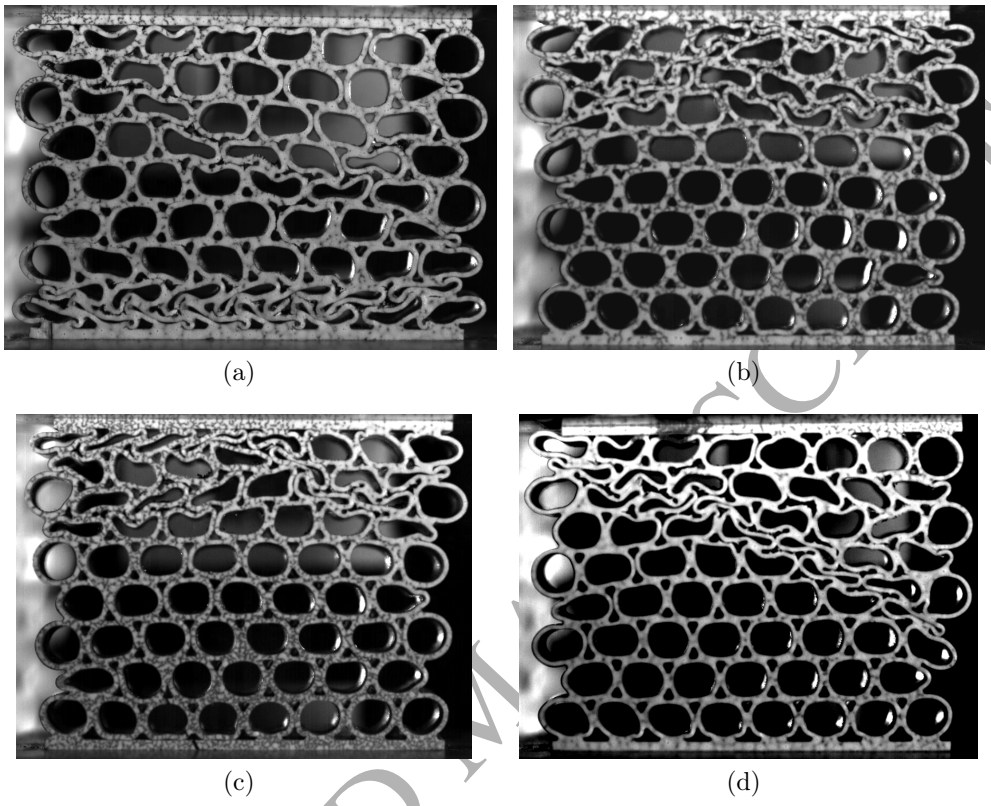

Figure 7: Local deformation observed at $E_{22} = -0.27$ for the hexagonal stacking core specimens: (a) H11 (b) H12 (c) H14 (d) H15.

Table 2: Mechanical properties of the cellular structure with the hexagonal stacking core.

Test number	E_{ef} MPa	$-\Sigma_0$ MPa	$-\Sigma_c$ MPa	$-E_c$.	W_c MPa	$-E_t$.	W_t MPa
H11	2354	60.1	57.7	0.430	23.4	0.430	23.4
H12	3772	61.1	57.2	0.445	24.9	0.445	24.9
H14	3661	62.5	52.9	0.433	21.4	0.433	21.4
H15	4284	61.2	56.6	0.426	23.1	0.426	23.1
average	3518	61.2	56.1	0.433	23.2	0.433	23.2

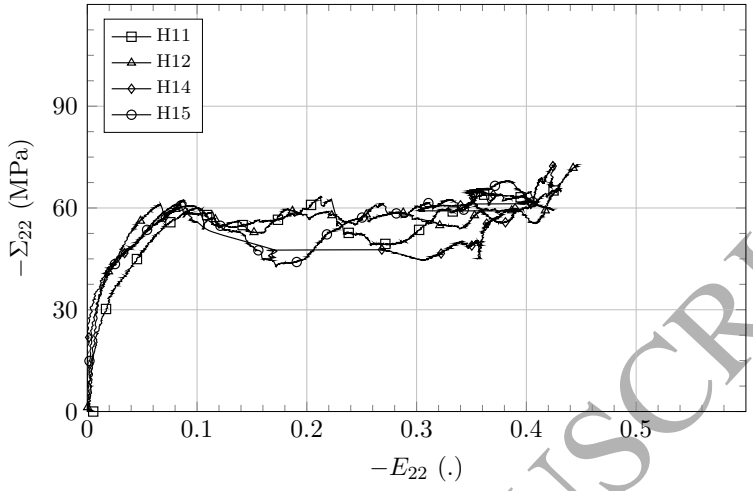

Figure 8: Nominal stress - nominal strain diagrams obtained for the hexagonal stacking core.

(square or hexagonal). The confinement was beneficial for the hexagonal stacking. The difference between the elastic modulus of both stacking cores was much larger in the case of confined tests compared to the unconfined ones. Papka and Kyriakides (1998) have performed unconfined compression tests on the hexagonal stacking only and a simple shear band was observed. In the experiments presented in this paper, the compressions tests were unconfined and a X-shear band was observed for the square stacking core while a simple shear band, comparable to that of Papka and Kyriakides (1998), was observed for the hexagonal stacking core.

Shim and Stronge (1986) have observed also that the first tubes to collapse were located next to the skins (Fig. 6). This was because the brazed joints were less numerous in the hexagonal stacking between the tubes and the skins compared to the number of brazed joints within the core. The brazed joints being less numerous in the square stacking core, the elastic modulus of the hexagonal stacking was greater than that of the square stacking one. This was confirmed by the computations of Iltchev et al. (2015). The specimens tested by Papka and Kyriakides (1998) were manufactured with no top and bottom skins. A simple, narrow, shear band was clearly developing within the core in that case (no additional shear band next to the skins). The deformation process was very repeatable and created a stress plateau with

undulations, less irregular compared to the results in Fig. 8.

In the case of stacked tubes in contact only (Shim and Stronge, 1986), plastic hinges were located at the inter-tube contact points and at points mid-way between them. In the case of brazed stacked tubes, plastic hinges were on both sides of the brazes and mid-way between the brazes.

Many analytical models in the literature assume that the density is the main parameter governing the mechanical properties of cellular structures (Gibson and Ashby, 1982, 1997). Here, both the hexagonal and square stacking cores have very similar equivalent densities (2.6910^{-3} g.mm^{-3} and 2.8910^{-3} g.mm^{-3} for the square and hexagonal stacking cores), but their mechanical properties are very different due to the cellular architecture.

The effective elastic modulus of the square stacking was approximatively half that of the hexagonal one. The yield and collapse stresses obtained with the square stacking were about one third of those of the hexagonal one. The total energies W_t given in Tables 1 and 2 were obtained for almost identical values of nominal strain, 0.45 and 0.43 for the square and hexagonal stacking cores respectively. The total energy dissipated by the square stacking was about 40% of the hexagonal one. As mentioned previously, the total energy for the square stacking was computed with the consolidation of the structure taken into account. On the contrary, the tests with the hexagonal stacking cores were stopped before the consolidation stage had started. Moreover, the collapse energy W_c given in Tables 1 and 2 were obtained for different values of collapse strain E_c (0.35 and 0.43 for the square and hexagonal stacking cores respectively). It is shown in Table 3 that, when normalized ($W_c^1 = -W_c/E_c$), the collapse energy for the square stacking was about one third of that of the hexagonal stacking.

This disagreement with the models of the literature can be explained by the fact that the number of neighbours for each tube is not the same for the hexagonal and square stackings. Each tube in the hexagonal stacking has six braze joints (instead of only four for the square stacking) which stiffen the tube walls, hence an increased resistance to compression.

The compression tests have shown for both stacking cores very large deformations, displacements and rotations, and also many contact points. The deformation of the structures under compressive load is consequently very challenging to simulate. To this aim, a contact algorithm developed for bi-parabolic elements and implemented in the explicit software package is first presented.

Table 3: Normalized collapse energy.

Test number	$-E_c$.	W_c MPa	W_c^1 MPa	Test number	$-E_c$.	W_c MPa	W_c^1 MPa
C10	0.347	6.82	19.6	H11	0.430	23.4	54.4
C11	0.348	6.64	19.1	H12	0.445	24.9	55.9
C12	0.363	6.20	17.1	H14	0.433	21.4	49.4
C14	0.346	6.92	20.	H15	0.426	23.1	54.2
average	0.351	6.64	18.9	average	0.433	23.2	53.5

3. Pinball contact-impact method

The cellular structures tested under compressive loads are subjected to many contacts during the deformation process. Contact algorithms are also an important component of numerical simulation software in fast transient dynamics. Such algorithms have been traditionally based on the so-called sliding lines and sliding surfaces (Hallquist et al., 1985). Sliding-based algorithms may present some difficulties in detecting contacts in complex geometrical situations. Therefore, an alternative formulation based on the so-called pinball metaphor has been proposed by Belytschko and Neal (1991) and Belytschko and Yeh (1993). This approach is more robust in detecting contacts. The details on the development of the contact algorithm compatible with bi-parabolic elements are given in the Appendix A for the sake of brevity. Only the base-line of the pinball method is reminded in the following paragraphs.

In the pinball method used in ∈PX, a computer program for the Finite Element simulation of fast dynamic phenomena, the user defines the elements that may enter in contact with one another and a 'parent' pinball (a sphere for 3D problems or a circle for 2D problems) is associated with each one of these elements. The centre of each pinball is simply the average of the nodal positions of the associated element. By default, the radius of the pinball is computed so as to encompass all nodes of the element in the current configuration. While the pinball radius is kept constant, by assuming that element deformation is not too large and occurs (plastically) at constant volume, the centres of the pinballs are calculated at every time step.

Interpenetration is checked by comparing the distance of the centres of two pinballs with the sum of their radii. If interpenetration of a couple of

pinballs is detected, equal normal velocity is enforced at the relevant nodes by the method of Lagrange multipliers and the corresponding contact forces are computed (Fig. 9). It is worth noting that the distinction between master and slave pinballs, that is maintained by Belytschko and Neal (1991) for historical and practical reasons, is rather artificial. In fact, the pinball algorithm is inherently symmetric and no distinction is needed *a priori* between a master and a slave (unlike in sliding surface and sliding line methods).

A set of pinballs forms one body that may come in contact with other bodies. Normally, contact between pinballs belonging to the same body is not checked. However, the contacts that may occur inside the tubes are typical of the so-called 'auto-contact' or 'self-contact' conditions. In this case, thanks to a special input command contact is also checked different pinballs belonging to the same body.

Sometimes the representation of an element by just one (parent) pinball is geometrically crude. Optionally, contact may be verified on a hierarchy of 'descendent' pinballs derived from the parent pinballs described above by recursively halving (upon to a certain level or to a certain size specified by the user) the pinball dimensions. This allows finer spatial resolution of the contact conditions. A parent (0-level) pinball is associated with each element. Then, the pinball radius is roughly divided by two at each new level produced as shown in Fig. 9.

By default, the radius of any descendent pinball is computed so as to encompass all 'nodes' of the corresponding element portion in the current configuration. Optionally, the radius of final-level descendent pinballs may be computed in such a way that their volume equals the initial volume of the associated element portion. This further increases slightly the accuracy of contact detection.

The pinball method is applied to the cellular structures tested under compressive load. The next section illustrates the models used to simulate the tests and to investigate the influence of the type of elements (i.e. quadrangular, triangular, linear, quadratic) and the type of numerical scheme (i.e. implicit or explicit) on the mechanical behaviour of the structure.

4. Finite Element Analysis

The square and hexagonal stacking cores were modelled with implicit static code *Z-set* and explicit fast-transient dynamic code €PX. Since the problem

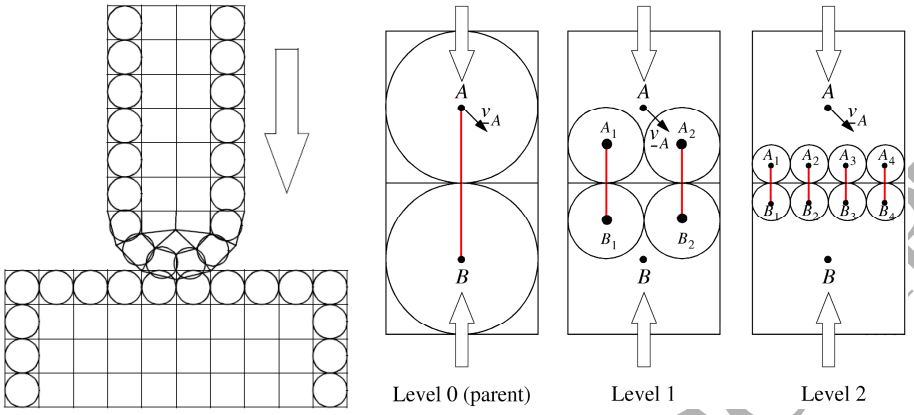

Figure 9: Pinball contact-impact method: general principle on the left, hierarchy pinball levels on the right (picture taken from Belytschko and Neal (1991)).

presented here is practically static, it can be anticipated that its solution with an explicit fast-transient dynamic code such as €PX will be expensive in terms of CPU time. The cellular structures have been subjected to quasi-static compressive loading conditions. In future works that are not reported here, these cellular materials will be tested under compressive impact loads, for which €PX is much better suited. There is therefore an interest to compare the numerical results obtained in quasi-static loading conditions from the different computational methods implemented in implicit static code *Z-set* and explicit fast-transient dynamic code €PX when using the same type of elements and the same mesh grid.

4.1. Material properties

The tubular specimens, with the dimensions given in Fig. 10, were made of Inconel® 600 material. After the tubes were machined, each specimen was submitted to NiP layer coating and then subjected to the same heat treatments as in the brazing and annealing processes (section 2.1). Tensile tests were performed to characterise the material isotropic hardening (Portemont et al., 2014). Experimental results have shown that the isotropic hardening could be modelled with the Ramberg-Osgood constitutive law presented in Eq. (1).

$$\sigma = \sigma_0 + Cp^n \tag{1}$$

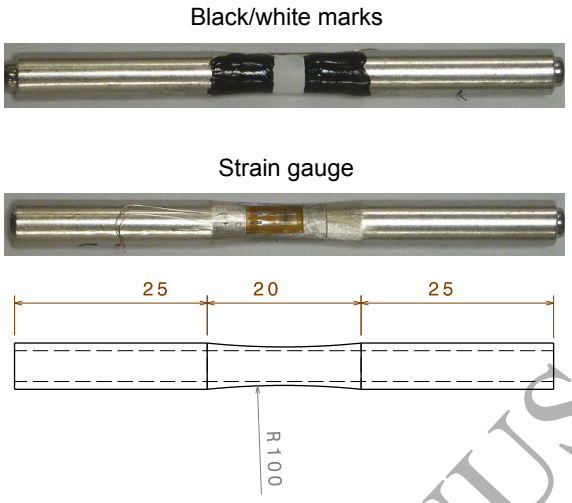

Figure 10: Tubular specimen for tensile tests. The dimensions of the specimen are given in mm and the external diameter in the thinner central part of the tube is 5 mm. The strain is measured on one side of the specimen by the optical extensometer with the black/white marks, and on the other side a gauge is bonded.

where p is the cumulative plastic strain, σ_0 is the initial yield stress. C and n are the isotropic hardening modulus and exponent, respectively.

The model parameters were determined thanks to the true-stress - true-strain diagrams obtained for the different tests performed under quasi-static tension ($2\,\mathrm{mm.mn^{-1}}$) and for plastic strains up to 0.2. (The necking starts for plastic strains above 0.2.) The model parameters, $\underline{z} = \{\sigma_0, C, n\}$, were identified using a numerical optimisation procedure based on a Simplex algorithm with the cost function f defined by relation (2), which is the quadratic sum of errors made for each experimental data point. In relation (2), $d(i)$ stands for the distance, for a given plastic strain p_i between the constitutive model, $\sigma(\underline{z}, p_i)$, and the corresponding experimental data, $\sigma_{exp}(i)$.

$$f(\underline{z}) = \sum_{i=1}^{N} \frac{d(i)^2}{\sigma_{exp}(i)^2} = \sum_{i=1}^{N} \frac{(\sigma(\underline{z}, p_i) - \sigma_{exp}(i))^2}{\sigma_{exp}(i)^2} \tag{2}$$

The following values were identified for the model parameters:

- elastic properties: $E = 197600\,\mathrm{MPa}$, $\nu = 0.29$,

- initial yield stress: $\sigma_0 = 252\,\text{MPa}$,
- isotropic hardening properties: $C = 1697\,\text{MPa}$ and $n = 0.71$.

These material constants were used in the following FE simulations using *Z-set* or €PX software packages. One should note that the material density was set to $8.25\ 10^{-3}\,\text{g.mm}^{-3}$ for the computations performed with explicit FE code €PX.

4.2. Geometry and FE meshing

The dimensions of the structures, the diameters of the tubes and the thickness of the skins were already given in section 2.1. The cellular structures were modelled with 2D plane-strain elements for cost efficiency.

In €PX only quadrangular elements and a polar decomposition for the finite strain formulation were available. Four-node quadrangular finite elements with linear shape functions are commonly used by €PX users for continuum-like elastoplastic solids subjected to impact loads, although nine-node finite elements with quadratic shape functions are more accurate. However, when using elements of the same size, the time step (for computational stability) of 9-node elements is half that of 4-node elements, and the number of degrees of freedom is higher. For these both reasons, the computational cost with €PX is higher when using parabolic 9-node finite elements than with linear 4-node finite elements.

The size of the element used in the computations with the quadrangular finite elements was about 0.125 mm (4 FE through the tube wall thickness). This size was determined thanks to a mesh convergence parametric study performed on single tube lateral compression using bi-parabolic elements. FE simulations were performed with meshes varying from 1 FE to 8 FE per tube wall. The results showed that the global responses and the deformation modes were well predicted when the tube had at least 4 FE per wall. Of course, FE results with more than 4 FE per wall were better, but the stability time step of the explicit scheme became too small for the modelling of the cellular structures. The numbers of nodal points and finite elements are given in Table 4. The FE models implemented for the square stacking core and the hexagonal stacking core are presented in Fig. 11.

(a) (b)

Figure 11: Quadrangular FE Meshes for the tested cellular structures. (a) square stacking core (b) hexagonal stacking core.

In *Z-set* both quadrangular and triangular elements were implemented as well as both polar and co-rotational decompositions. Different meshes were considered, the quadrangular one used for explicit simulations (Fig. 11) and a triangular one with refined elements in the neighbourhood of the braze joints (Fig. 12). Whereas for quadrangular meshes only a polar decomposition was used for the finite strain formulation, for triangular meshes either a polar or a co-rotational decomposition was used. The numbers of nodal points and finite elements are given in Table 4. For the triangular meshes, the choice of three elements in the thickness of the tubes resulted from our previous works on hollow-sphere (Marcadon and Feyel, 2009; Marcadon and Kruch, 2013) and tube (Marcadon et al., 2012; Marcadon and Kruch, 2011) stackings which have shown that calculations converged in terms of element size for such refined meshes.

Since the cellular structures tested in this paper were subjected to large compaction levels, involving large strains and rotations, a full-integration formulation was applied. The comparisons between the predictions from both €PX and *Z-set* software packages were performed in terms of both element type and size and finite strain formulation.

4.3. Contacts and initial conditions

In €PX, the internal contact was modelled by the pinball method (see section 3 and Appendix A) with the maximum hierarchy level set to 2 for a finer spatial contact resolution (to avoid spurious contacts in particular in the case of self-contacts). The radius of the pinballs generated in the hierarchic method was computed in such a way that its volume equalled the

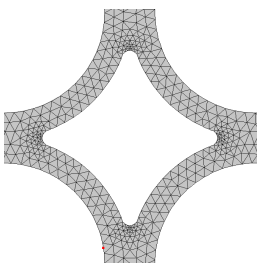

(a)

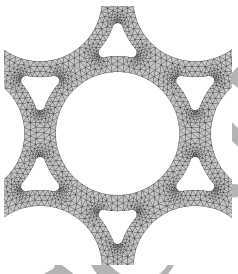

(b)

Figure 12: Triangular FE Meshes for the tested cellular structures (implicit simulations only). (a) square stacking core (b) hexagonal stacking core.

Table 4: Synthesis of the FE models for the tested cellular structures.

Computational FE model	Element type	Number of nodes	Number of FE (physical)	Number of Gauss points
Square stacking core	4-node linear	31658	26240	104960
	9-node quadratic	115922	26240	236160
	3-node linear	29100	48720	146160
	6-node quadratic reduced	107046	48720	146160
Hexagonal stacking core	4-node linear	34135	28736	114944
	9-node quadratic	125927	28736	258624
	3-node linear	34167	58332	174996
	6-node quadratic reduced	126851	58332	174996

initial volume of the associated element portion. These options delivered satisfactory results during the parametric study performed with a simplified model of cellular structure (Casadei et al., 2014b).

Different bodies for the pinball method were created for each self-contact zone in the FE models (e.g., inside each tube and between tubes, see Fig. 13 for the square stacking core) for cost efficiency. It should be noted that defining a single self-contacting zone would give identical results. The numbers of local (parent) pinballs were 8708 and 8526 for the FE models of the square and the hexagonal stacking cores, respectively.

In *Z-set*, the internal self-contact was modelled in implicit by using classical frictionless Coulomb contact without any penalty condition.

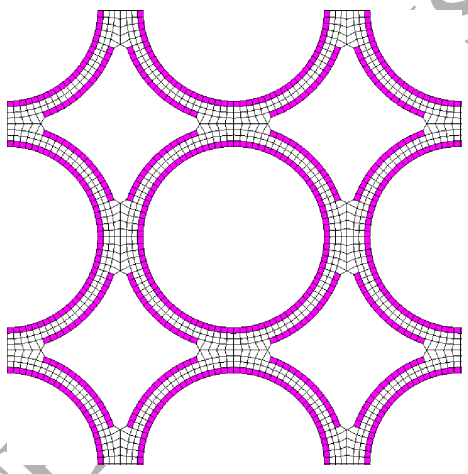

Figure 13: Self-contact zones for the pinball contact-impact method and the square stacking core.

The anvils were not implemented in the simulation to model the anvil/top skin and anvil/bottom skin contact conditions because no friction model was compatible yet with the pinball method in €PX and the Coulomb contact in *Z-set* was chosen frictionless. A vertical displacement U_2 was consequently prescribed for the nodal positions of the bottom and top skins. The bottom skin was blocked: $U_2 = 0$. The top skin was subjected to an imposed displacement: $U_2 = 20\,\text{mm}$ at the end of the computation (the final physical time of calculation was 20 ms with €PX), corresponding to a final expected

nominal strain of $E_{22} = -0.48$. The node located at the centre of the bottom skin was blocked in the horizontal direction ($U_1 = 0$).

4.4. Numerical results

The computations with €PX were performed on a computer cluster using 8 threads and the following performances: Intel® Ivy-Bridge E5-2667v2 @ 3.29 GHz, 132 GB RAM, 10 GB swap. The computations with *Z-set* were performed on computer clusters using 4 threads and the following performances: AMD® Opteron Magny-Cours 6176 SE @ 2.3 GHz, 72 GB RAM.

For a sake of briefness and because similar collapse modes were predicted by both explicit and implicit simulations, contour plots are presented only from €PX (see Appendix B).

The computed nominal stress - nominal strain responses are presented in Fig. 14. There was a very good agreement between the predictions of both FE codes, explicit one €PX on one side and implicit one *Z-set* on the other side. The mechanical responses were very close for a given order of the meshes (i.e. linear or quadratic), whatever the element type (i.e. triangular or quadrangular) and the finite strain formulation (i.e. polar or co-rotational).

Papka and Kyriakides (1998) have shown that the computed responses remained monotonically increasing when the stacking deformed symmetrically. This was particularly true for the computations presented in this paper using linear elements and the square stacking that deformed symmetrically (Fig. B.19, see Appendix B).

The mesh order had a very important influence on the numerical nominal stress - nominal strain responses. The model made with linear elements were too stiff whatever the element type and the mesh refinement in the braze joint areas. The convergence of linear mesh was studied with €PX and the model of the square stacking core using a refined 4-node elements mesh. The mesh refinement had consisted in splitting each element of the initial mesh (Fig. 11(a)) in two in each direction. The computational results were improved by refining the linear mesh. However, the computed response with the refined mesh still largely differs from the data obtained with the parabolic FEs.

The local plastic strains obtained for both stackings are presented in Figs. B.19 and B.20 (see Appendix B) for the the linear and quadratic meshes respectively. The mesh order had a very important influence on the local responses

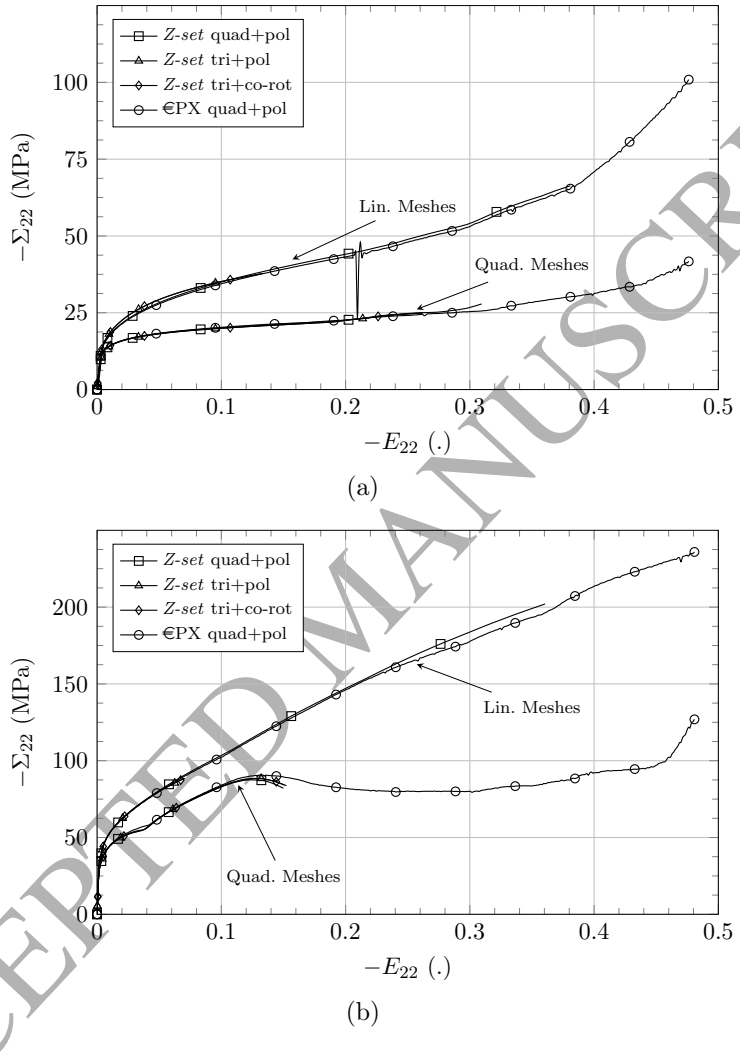

Figure 14: FE predictions of nominal stress - nominal strain responses: comparison between the two FE codes evaluated and the FE formulations (a) for the square stacking core (b) for the hexagonal stacking core. When referring to meshes the abbreviation quad. means quadratic, whereas it means quadrangles when it refers to the element geometry.

of the models. A simple shear band, comparable to the computations by Papka and Kyriakides (1998), was initiated in the hexagonal stacking when the model was set up with quadratic elements. The horizontal displacement of the top skin was very different depending on the mesh order. When using linear meshes, it was almost zero in the case of the square stacking and was larger in the case of the hexagonal stacking. The tubes collapsed and the local strains were more localised within the folds or plastic hinges, when the computations were performed with quadratic meshes. This was particularly true for the hexagonal cellular structure; tubes collapsed row after row and the cells were almost closed at the end of the computations.

For the explicit FE code, the stability time step decreased significantly during the computations. However, this was typical of solid structure computations under large compression levels. No numerical instability was observed and every computations were successfully performed until the physical time prescribed in the input file. Implicit simulations needed considerably longer computation durations compared with the explicit ones and their convergence was more difficult because of some geometrical locking of the elements around braze joints. Thus, even after several weeks of computation (few months for some cases), the compaction levels reached from implicit simulations remained significantly lower than those reached from explicit ones.

5. Discussions

The models made of linear elements did not reproduce well the experimental data. For the quadratic meshes, the type of element had a very limited influence on the nominal stress - nominal strain responses and also on the local deformations. Only the results from the code €PX obtained with the quadratic meshes (quadrangular elements) are compared in this section with the experimental data. The tests were stopped when the consolidation of the structure started (to avoid exceeding the load capacity limits of the experimental set-up). Computational results are given over this range to assess the numerical stability over a compaction level of 50%, especially during the consolidation of the structure.

First, the top skin of the cellular structures was free to move in the horizontal direction. The experiment did not exhibit such large horizontal displacements of the top skin. In the experiments, the development of X-shape shear bands had prevented such horizontal displacement in the case of the square

stacking structures (see Fig. 3). Such horizontal displacement was observed in the deformation mode of the hexagonal stacking structure shown in Fig. 7(d) which was close to the model (Fig.B20(b)). The nominal stresses were overestimated by the models, especially for the hexagonal stacking (Fig. 15).

Then, the FE models were also re-computed by blocking the horizontal displacement of the node located at the central position of the top skin. For the square stacking, the rotations of some braze joints located near the skins were larger in that case. The model did not reproduce well the X-shape shear bands. In the case of the hexagonal cellular structure, the position and the orientation of the first row that collapsed were different. The nominal stress - nominal strain responses were not significantly affected by this change in the boundary conditions.

As already mentioned, most of the tubes in the models collapsed within the core and many were completely closed. Large plastic strain developed in the tubes and the maximum values were in the hinges. However, the braze joint zones were not subjected to strong plastic strains. With *Z-set*, triangular meshes were refined in the braze joints (compared to the quadrangular meshes), but this refinement had very limited influence on the numerical responses (both local and global).

The stronger overestimation of the nominal stress - nominal strain responses observed in the case of the hexagonal stacking might be explained by the fact that, experimentally, this stacking exhibited a more scattered and irregular behaviour than that of the square stacking because of more numerous stacking defects, such as missing braze joints and tube misalignment, which were not modelled. In the computations of Papka and Kyriakides (1998), a numerical instability was initiated at approximately the same row as in the experiment. This instability influenced the deformation of the pattern but not the overall response of the specimen. Moreover, some braze joints failed during the compression of the structure but failure was not modelled in the simulations. Consequently, the stress increase, induced by internal self-contact occurrence, was more spread experimentally than that predicted numerically.

In the present work, the Inconel® 600 material was characterized considering the effects of the process used to manufacture the cellular structures. Thus, the mechanical material properties were consequently correctly known and defined for the tubes. However, the issue of the mechanical properties of the brazes is more complex. This material differs from that of the tubes

in terms of composition and microstructure (Davoine et al., 2014), hence its mechanical properties are probably different. They cannot be characterised easily. Some previous works on tube stackings (Marcadon et al., 2012) investigated this issue by introducing a specific behaviour and damage into the braze, but the effect was rather limited. On the contrary, our previous works on hollow-sphere stackings (Marcadon and Feyel, 2009; Marcadon and Kruch, 2013) suggested that the geometry of the brazes and the existence of some geometrical defects is a more critical issue.

The numerical analysis of the influence of defects would need a fully parametric description of the geometry of the structures and also of the defects. This model is not available for the moment. To verify if defects could have an important influence on the numerical results, the authors tentatively modified the models of the cellular structures by affecting a weakened material to the FE of the braze joints (the material model of section 4.1 was previously affected to all FE of the models). The Young's modulus of the braze joint material was arbitrarily taken 10 times less than that of the tubes and skins. All other material properties were unchanged. This modification simply involved larger elastic strains for the same stress state.

The influence of the mechanical behaviour of the braze joints was very limited in the case of the square stacking core. The deformation of the structure was slightly modified, as shown in Fig. B.21, but the local plastic strains were not significantly increased in the braze joints. At the same compaction level, the horizontal displacement of the top skin was however less when the model was set-up with the weakened material law for the braze joints (see Figs.B.20(d) and B.21(c) for a compaction level of -0.42). The mechanical behaviour of the braze joints had a little influence of the nominal stress - nominal strain response of the square stacking core structure (Fig. 15(a)). The response of the FE model with the weakened material law affected to the braze joints was a little lower. The percentage difference between both models was almost constant during the deformation process of the structure (-7.5%).

The influence of the mechanical behaviour of the braze joints was much more significant in the case of the hexagonal stacking core. The deformation of the structure showed different mechanisms, because the braze joints experienced larger plastic strains in the model (see Figs.B.20(b) and B.21(a) for a compaction level of -0.24). This can be explained by the fact that, the brazes being more numerous compared with the square stacking, they

stiffen considerably the tubes and their contribution to the overall behaviour of the stacking is important. On the contrary, for the square stacking it is the tubes behaviour that governs the overall behaviour of the structure. The nominal stress - nominal strain response was significantly affected when the weakened material law was considered for the braze joints (Fig. 15(b)). A percentage difference of -30% was progressively reached for a nominal strain of -0.16. This maximum difference was almost constant until a nominal strain of -0.26 and differences between -10% and -30% were observed for a nominal strain above -0.16.

It is worth noting that, to go further it might be interesting to weaken only one or few brazes each time to investigate the influence of the distribution of the defects on the overall behaviour and the collapse modes. Indeed, some previous works have shown that particular distributions of the weakest elements towards the loading direction are more detrimental to the overall behaviour of the structure (Marcadon and Kruch, 2013; Silva and Gibson, 1997).

The introduction of a weakened material law did not affect the numerical stability of the models. The numerical results showed that the braze joints have a more important influence on the mechanical response of the hexagonal stacking. This conclusion was anticipated experimentally because the braze joint defects affected more the mechanical responses (both local and global) of the hexagonal stacking core.

6. Conclusion

This work aimed at studying the mechanical behaviour of cellular structures made of tube stackings under compressive loads. Experimental results have shown that the crushing behaviour of the square stacking core is a very stable process. The mechanical response has a very smooth and flat plateau even though defects are present in the cellular specimens. The deformation process of the hexagonal stacking core being more influenced by initial defects in the core, the mechanical response was consequently more chaotic during the crushing process. Both the hexagonal and square stacking cores had very similar equivalent densities, but their overall mechanical properties were very different due to the cellular architecture.

The compression tests have shown for both stacking cores very large deformations and displacements and also many contact points. The deformation

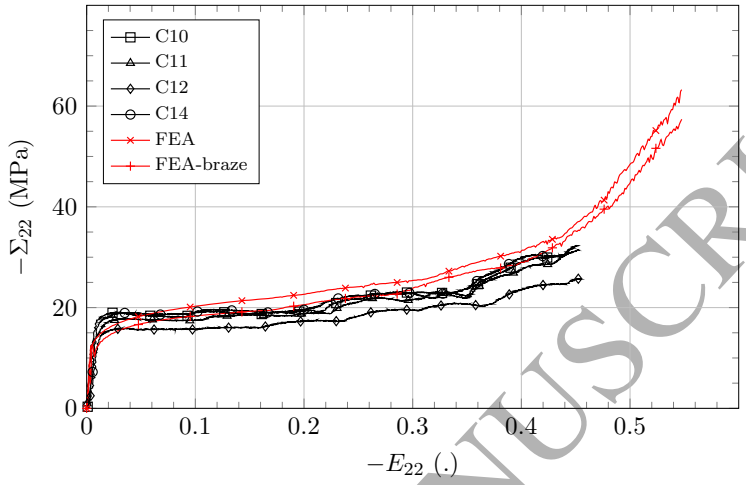

(a)

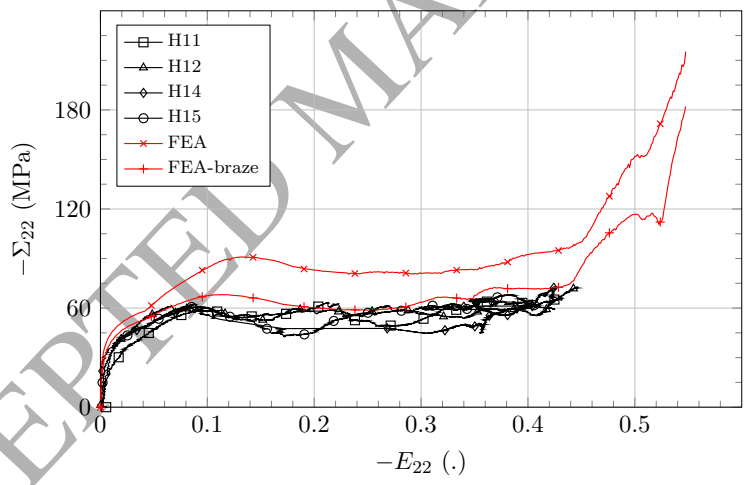

(b)

Figure 15: Comparison of nominal stress - nominal strain responses: (a) for the square stacking core (b) for the hexagonal stacking core. The influence of the braze joints mechanical behaviour on the nominal stress - nominal strain responses is given by the curves FEA-braze.

of the structures under compressive load is consequently very challenging to simulate. To this aim, a pinball contact algorithm compatible with bi-parabolic element has been implemented in the explicit software €PX and validated for all quadratic elements available in the FE code.

The models used to simulate the tests and to investigate the influence of the type of elements and the type of numerical scheme (implicit with *Z-set*, explicit with €PX) on the mechanical behaviour of the structure were presented. Results on both the square and hexagonal stacking cores have been presented and compared with the experimental data. A very good agreement between the predictions of both FE codes, explicit (€PX) on one side and implicit (*Z-set*) on the other side, was found. The computational results were very dependent upon the FE order implemented in the cellular structure. The nominal stress - nominal strain response obtained with the models made of linear FE was always greater than the one given by the models with parabolic elements. This result was particularly true for the hexagonal stacking core cellular structure that behaved completely differently depending on the type of elements implemented in the model. For a given order of the elements, both codes gave very close predictions whatever the geometry of the elements or the finite strain formulation. Compared with the experimental results, the relevance of the FE model was discussed. A better agreement was achieved between the predictions of the parabolic elements and the experimental results when the braze joint defects were tentatively introduced in the FE models by using weakened material properties.

Acknowledgement

This work has been supported by Onera in the framework of the Carnot institutes. We are indebted to our colleagues F. Popoff and C. Davoine for the processing of the samples.

Appendix A. Computational aspects of the Pinball method in €PX

The pinball contact-impact method has been implemented in the FE code €PX initially based upon a 'strong' (coupled, implicit) Lagrange multiplier solution strategy of the contact constraints (Casadei, 2002). Recently, an alternative penalty-based (fully explicit) solution of the contact constraints has been introduced by Casadei et al. (2014a) as an option in the code.

Following Belytschko and Neal (1991) and Casadei (2003a), the penetration can be calculated as follows. Consider two interpenetrating pinballs, 1 and 2, as shown in Fig. A.16, with the velocities $\underline{v}_1$ and $\underline{v}_2$; the normals of the associated surfaces are $\underline{n}_1$ and $\underline{n}_2$. The position vectors of the two pinballs are given by $\underline{C}_1$ and $\underline{C}_2$. The interpenetration is given by g and is defined as the relative displacement of the centers of the pinballs in the average direction $\underline{n}$ needed to eliminate the interpenetration (see relations (A.1) and (A.2)). The average normal direction is given by the relation (A.3).

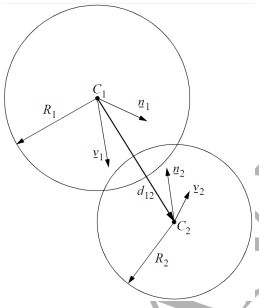

Figure A.16: Interpenetration of two pinballs (picture taken from Belytschko and Neal (1991)).

$$\underline{d}^t \underline{d} = (R_1 + R_2)^2 \tag{A.1}$$

$$\underline{d} = \underline{C}_1 - \underline{C}_2 + g\underline{n} \tag{A.2}$$

$$\underline{n} = \frac{\underline{n}_2 - \underline{n}_1}{\|\underline{n}_2 - \underline{n}_1\|} \tag{A.3}$$

where $\| \ \|$ is for the length of a vector.

The penetration g can be determined by relations (A.4) and (A.5). Note that only the positive radicand in the relation (A.4) needs to be considered. The negative root corresponds to a negative value of g which is irrelevant. Besides the interpenetration g, the rate of penetration $\dot{g}$ may be computed following relation (A.6).

$$g = -b + \sqrt{b^2 - c} \tag{A.4}$$

where b and c are defined by:

$$\begin{aligned} b &= \underline{n}^t \left(\underline{C}_1 - \underline{C}_2\right) \\ c &= \|\underline{C}_1 - \underline{C}_2\|^2 + (R_1 + R_2)^2 \end{aligned} \tag{A.5}$$

$$\dot{g} = \frac{\Delta g}{\Delta t} = \frac{1}{N} \sum_{i=1}^{N} \left(\underline{v}_i^{(2)} - \underline{v}_i^{(1)}\right) \cdot \underline{n} \tag{A.6}$$

where $\underline{v}_i^{(j)}$ are the nodal velocities ($i \in \{1, N\}$, with N the number of nodes) of element j. Note that the quantity g can also be considered to be given by the time integral of $\dot{g}$ (A.7). In a surface-based slide-line algorithm, $\dot{g}$ is not path-independent.

$$g = \int_{t_1}^{t} \dot{g} dt \tag{A.7}$$

where t_1 is the time when penetration begins.

Note that the calculation of the penetration amount is only needed when the penalty-based approach is adopted for the calculation of the contact forces. The Lagrange multipliers approach only needs a check of whether or not there is interpenetration, but the amount of the latter is irrelevant. A more detailed algorithm than the one summarised above for the calculation of the penetration, used in conjunction with the penalty approach and the ASN algorithm, is reported by Casadei et al. (2014a), and is not presented here for the sake of brevity.

Besides the detection of contact (interpenetration) conditions presented in the previous paragraph, any contact-impact algorithm requires the determination of suitable contact forces, acting on the touching bodies and preventing (further) interpenetration of the two domains. Belytschko and Neal (1991) present two implementations of contact force determination for the pinball algorithm, one based on the penalty method and the other based on the Lagrange multipliers. In the latter case, contact forces should ensure the relation (A.8)

$$(\underline{v}_1 - \underline{v}_2) \cdot \underline{n} \leq 0 \tag{A.8}$$

where $\underline{v}_1$ and $\underline{v}_2$ are the velocities of the two pinballs and $\underline{n}$ represents a suitable normal direction to the contact surface. Note that relation (A.8) is an inequality and not an equation. The case with the $<$ sign corresponds to the

possibility of rebound and must be suitably treated in the implementation. Two alternative implementations of rebound, one based on an *a priori* estimation of rebound (this is the one used here) and the other on an *a posteriori* checking of the sign of the Lagrange multipliers, are implemented in €PX, but are not detailed here for the sake of brevity.

The contact condition (A.8) can also take the form given by relation (A.9) and the velocities at the two pinball centers are expressed by relations (A.10) and thus involve the velocities of all nodes of elements 1 and 2 through suitable shape functions N. The unit normal $\underline{n}_{12}$ is directed along the line joining the two pinball centers and is oriented from 1 towards 2. A problem is to determine the normalised coordinates of the pinball centers to compute $N_{1i}(1)$ and $N_{2i}(2)$ in relations (A.10). $\underline{v}_{1i}$ and $\underline{v}_{2i}$ are given by the explicit integration scheme.

$$\underline{v}_1 \cdot \underline{n}_{12} - \underline{v}_2 \cdot \underline{n}_{12} \leq 0 \tag{A.9}$$

and

$$\underline{v}_1 = \sum_{i=1}^{n_1} N_{1i}(1)\, \underline{v}_{1i} \quad \underline{v}_2 = \sum_{i=1}^{n_2} N_{2i}(2)\, \underline{v}_{2i} \tag{A.10}$$

In Finite Element formulations use is often made of interpolations (mappings) of the form: $f(x) = \sum_{i=1}^{n} N_i(\xi)\, f(x_i)$, whereby the value of a function at a point in the space of global coordinates $\underline{x}$, usually lying within a finite element characterised by n nodal points i, is computed by a weighted interpolation of the function values at the nodal points $f(x_i)$ by means of appropriate shape functions N_i. These functions are usually expressed in terms of the so-called normalised coordinates ξ, that map the element or volume onto a parent element or volume. The inverse mapping problem consists in finding the normalised coordinates of a point in space with respect to a known geometric figure (i.e an element). These methods have been developed and presented by Casadei (2001, 2003b) for elements with linear shape functions. The inverse mapping method is used to compute the normalised coordinates of the pinball centers based on their corresponding coordinates and then to compute the velocities at the pinball centers: $\underline{v}_1$ and $\underline{v}_2$ in relations (A.10).

The method developed for the bi-parabolic element in Fig. A.17 is similar to the one developed for the bi-linear quadrilateral element (Casadei, 2001, 2003b). The actual local numbering of the element nodes implemented in

€PX is the one given in Fig. A.17 in order to make it compatible with QUA9 element shape of Cast3m pre-processor (circular numbering). With the numbering of Fig. A.17, the shape functions are given by relations (A.11).

$$\begin{array}{ll} N_1(\xi,\eta) = \frac{1}{4}\xi\eta(\xi-1)(\eta-1) & N_5(\xi,\eta) = \frac{1}{4}\xi\eta(\xi+1)(\eta+1) \\ N_2(\xi,\eta) = \frac{1}{2}\eta(1-\xi^2)(\eta-1) & N_2(\xi,\eta) = \frac{1}{2}\eta(1-\xi^2)(\eta+1) \\ N_3(\xi,\eta) = \frac{1}{4}\xi\eta(\xi+1)(\eta-1) & N_7(\xi,\eta) = \frac{1}{4}\xi\eta(\xi-1)(\eta+1) \\ N_4(\xi,\eta) = \frac{1}{2}\xi(\xi+1)(1-\eta^2) & N_8(\xi,\eta) = \frac{1}{2}\xi(\xi-1)(1-\eta^2) \\ \multicolumn{2}{c}{N_9(\xi,\eta) = (1-\xi^2)(1-\eta^2)} \end{array} \tag{A.11}$$

The direct coordinate mapping is defined by:

$$x = \sum_1^9 N_i x_i \quad \text{and} \quad y = \sum_1^9 N_i y_i \tag{A.12}$$

and by developing relations (A.12) with relations (A.11), we get:

$$\begin{aligned} F_1(\xi,\eta) &= a_1\xi^2\eta^2 + b_1\xi^2\eta + c_1\xi\eta^2 + d_1\xi\eta + e_1\xi^2 \\ &\quad + f_1\eta^2 + g_1\xi + h_1\eta + i_1 - 4x = 0 \\ F_2(\xi,\eta) &= a_2\xi^2\eta^2 + b_2\xi^2\eta + c_2\xi\eta^2 + d_2\xi\eta + e_2\xi^2 \\ &\quad + f_2\eta^2 + g_2\xi + h_2\eta + i_2 - 4y = 0 \end{aligned}$$

with:

$$\begin{array}{l|l} a_1 = x_1 - 2x_2 + x_3 - 2x_4 + x_5 & a_2 = y_1 - 2y_2 + y_3 - 2y_4 + y_5 \\ \qquad - 2x_6 + x_7 - 2x_8 + 4x_9 & \qquad - 2y_6 + y_7 - 2y_8 + 4y_9 \\ b_1 = -x_1 + 2x_2 - x_3 + x_5 & b_2 = -y_1 + 2y_2 - y_3 + y_5 \\ \qquad - 2x_6 + x_7 & \qquad - 2y_6 + y_7 \\ c_1 = -x_1 + x_3 - 2x_4 + x_5 & c_2 = -y_1 + y_3 - 2y_4 + y_5 \\ \qquad - x_7 + 2x_8 & \qquad - y_7 + 2y_8 \\ d_1 = x_1 - x_3 + x_5 - x_7 & d_2 = y_1 - y_3 + y_5 - y_7 \\ e_1 = 2x_4 + 2x_8 - 4x_9 & e_2 = 2y_4 + 2y_8 - 4y_9 \\ f_1 = 2x_2 + 2x_6 - 4x_9 & f_2 = 2y_2 + 2y_6 - 4y_9 \\ g_1 = 2x_4 - 2x_8 & g_2 = 2y_4 - 2y_8 \\ h_1 = -2x_2 + 2x_6 & h_2 = -2y_2 + 2y_6 \\ i_1 = 4x_9 & i_2 = 4y_9 \end{array} \tag{A.13}$$

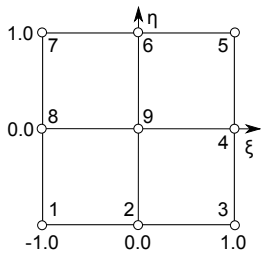

Figure A.17: Bi-parabolic 2D quadrilateral element.

System (A.13) being non-linear and not easy to be solved analytically, it is rather preferable to resort to a numerical solution obtained by the well-known Newton-Raphson iterative method. To this aim, the problem is formulated by posing:

$$\underline{\chi} = \begin{bmatrix} \xi \\ \eta \end{bmatrix} \text{ and } \underline{F}\left(\underline{\chi}\right) = \begin{bmatrix} F_1\left(\xi,\eta\right) \\ F_2\left(\xi,\eta\right) \end{bmatrix} = \begin{bmatrix} F_1\left(\underline{\chi}\right) \\ F_2\left(\underline{\chi}\right) \end{bmatrix}$$

The value $\underline{\chi}^\star$, such that $\underline{F}\left(\underline{\chi}^\star\right) = \underline{0}$, is sought with iterations of the Newton-Raphson method.

The velocity constraint for a contact between two parent (0-level) pinballs is written along a 'normal' direction which, by default, coincides with the line joining the two pinball centres (Fig. 9). For a contact between descendent pinballs (in the hierarchic method) one can alternatively use a 'common' normal (CNOR). One such normal is determined for each couple of contacting element faces. When multiple contacts between sub-pinballs occur in case of flat (face to face) element contact, the common normal is a better approximation than the standard one to the real contact direction.

The so-called Assembled Surface Normal (ASN) algorithm of Belytschko and Law (1985) may be optionally activated to compute an unique (normalised) normal to each external node of the mesh portion subjected to contact, and an unique (normalised) normal to each pinball (parent or descendent), as shown in Fig. A.18. The penetration direction between contacting pinballs is then computed using the ASNs of the two pinballs according to a set of rules. This improves the treatment of flat contact, especially in conjunction with a penalty formulation to compute the contact forces. ASN algorithm cannot be used together with CNOR method.

This method has been extended to all other linear and quadratic finite elements of FE code €PX. The implementation and the relevant test cases are reported by Casadei et al. (2014b).

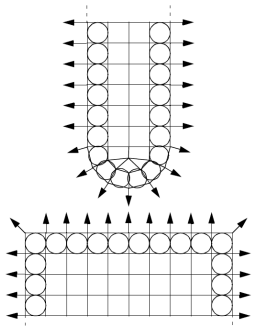

Figure A.18: Assembled surface normals (picture taken from Belytschko and Neal (1991))

Appendix B. Contour plots

This Appendix presents some contours plots of the cellular structures FE simulations. The pictures were obtained by the explicit fast-transient dynamic code €PX.

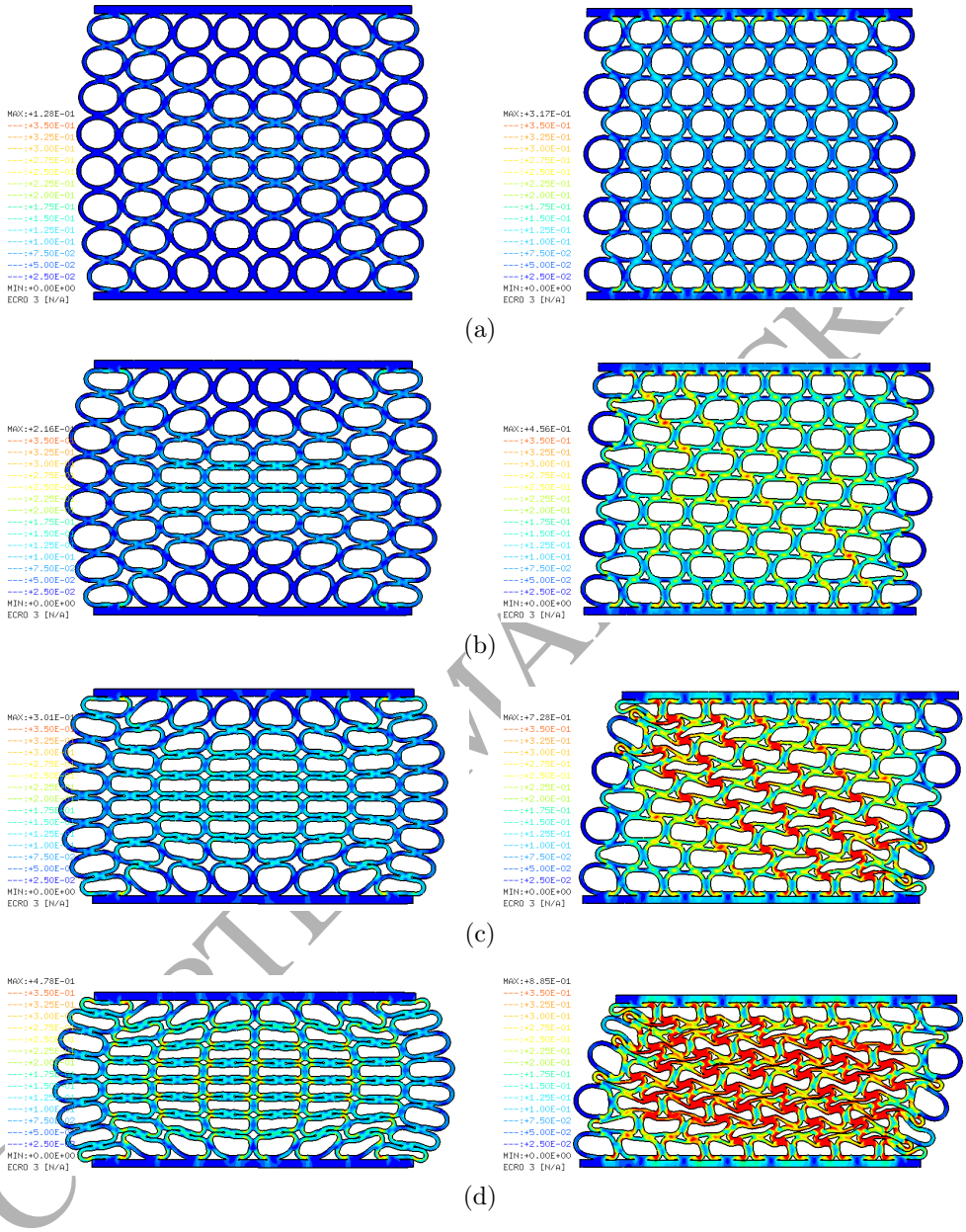

Figure B.19: Numerical deformation of the cellular structures (contours: cumulative plastic strain). The deformations were obtained with the meshes made of quadrangular linear FE. (a) $E_{22} = -0.12$ (b) $E_{22} = -0.24$ (c) $E_{22} = -0.36$ (d) $E_{22} = -0.47$.

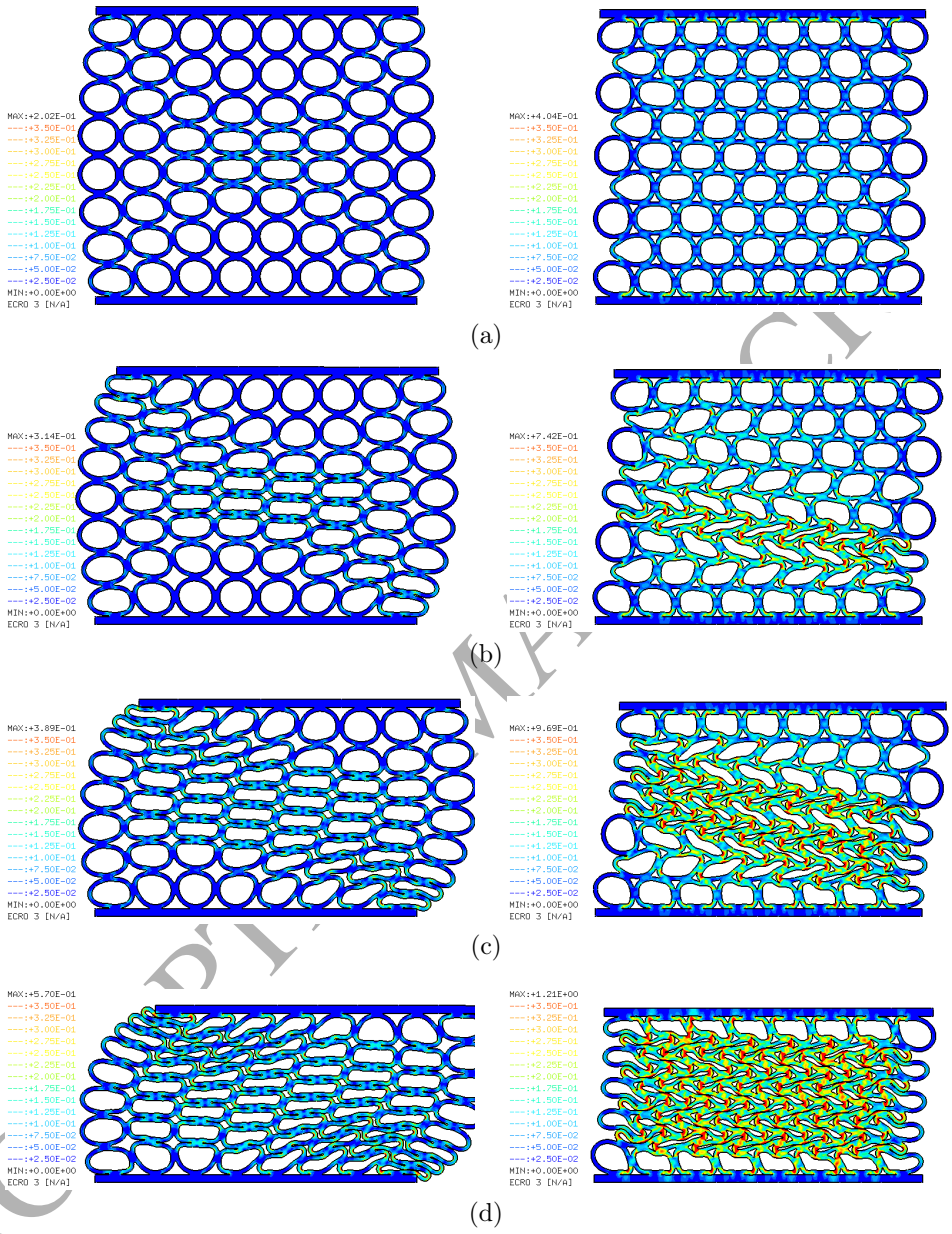

Figure B.20: Numerical deformation of the cellular structures (contours: cumulative plastic strain). The deformations were obtained with the meshes made of quadrangular biparabolic FE. (a) $E_{22} = -0.12$ (b) $E_{22} = -0.24$ (c) $E_{22} = -0.36$ (d) $E_{22} = -0.47$.

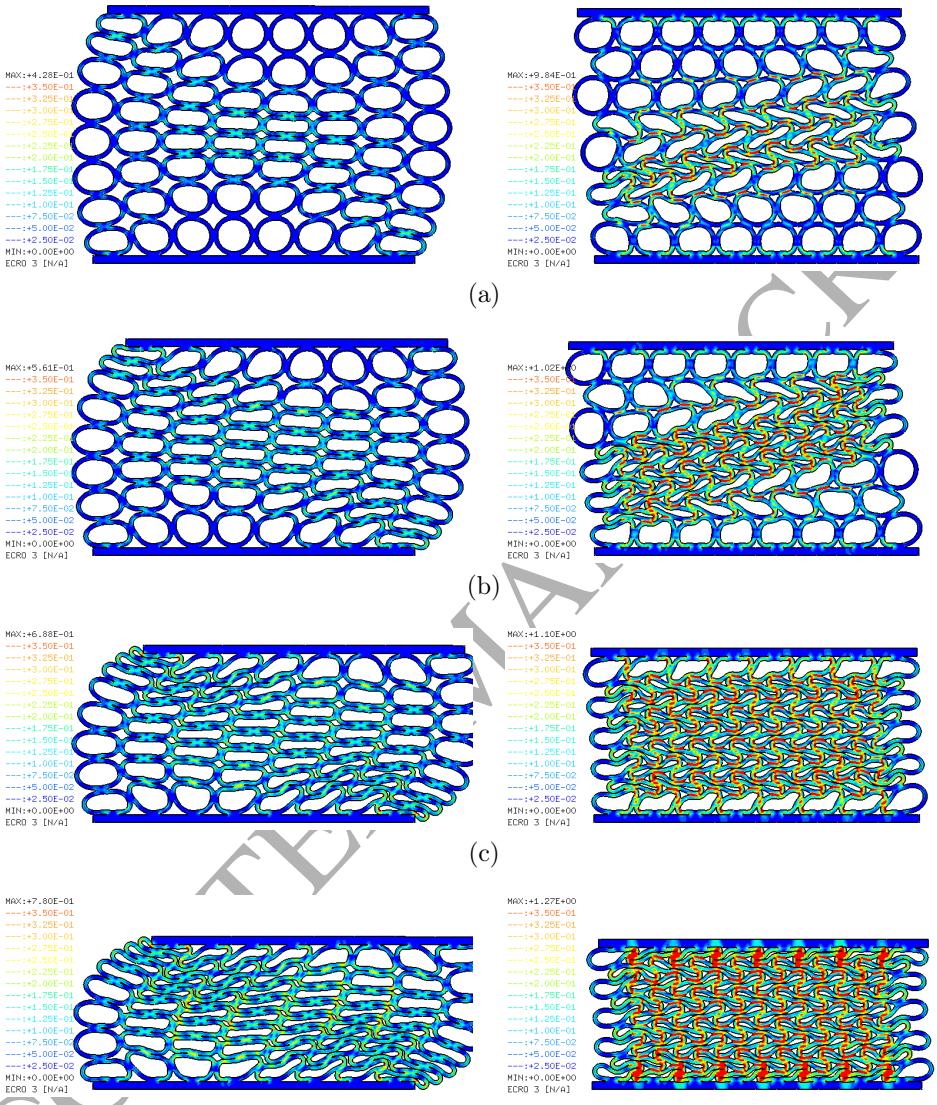

Figure B.21: Numerical deformation of the cellular structures (contours: cumulative plastic strain). The deformations were obtained with the meshes made of quadrangular biparabolic FE. The FEs of the braze joints were set-up with weakened material properties. (a) $E_{22} = -0.24$ (b) $E_{22} = -0.36$ (c) $E_{22} = -0.47$ (d) $E_{22} = -0.54$.

References

Alkhader, M., Vural, M., 2009. An energy-based anisotropic yield criterion for cellular solids and validation by biaxial fe simulations. Journal of the Mechanics and Physics of Solids 57 (5), 871–890.

Amsterdam, E., de Hosson, J. T. M., Onck, P. R., 2008a. On the plastic collapse stress of open-cell aluminum foam. Scripta Materialia 59, 653–656.

Amsterdam, E., de Vries, J. H. B., de Hosson, J. T. M., Onck, P. R., 2008b. The influence of strain-induced damage on the mechanical response of open-cell aluminum foam. Acta Materialia 56, 609–618.

Belytschko, T., Law, S., 1985. An assembled surface normal algorithm for interior node removal in three-dimensional finite element meshes. Engineering with Computers 1, 55–60.

Belytschko, T., Neal, M., 1991. Contact-impact by the pinball algorithm with penalty and lagrangian methods. International Journal of Numerical Methods in Engineering 31, 547–572.

Belytschko, T., Yeh, I., 1993. The splitting pinball method for contact-impact problems. Computer Methods in Applied Mechanics and Engineering 105, 375–393.

Blazy, J.-S., Marie-Louise, A., Forest, S., Chastel, Y., Pineau, A., Awade, A., Grolleron, C., Moussy, F., 2004. Deformation and fracture of aluminium foams under proportional and non proportional multi-axial loading: statistical analysis and size effect. International Journal of Mechanical Sciences 46 (2), 217–244.

Burteau, A., N'Guyen, F., Bartout, J.-D., Forest, S., Bienvenu, Y., Saberi, S., Naumann, D., 2012. Impact of material processing and deformation on cell morphology and mechanical behavior of polyurethane and nickel foams. International Journal of Solids and Structures 49, 2714–2732.

Casadei, F., December 2001. A module for inverse isoparametric mappings in europlexus. EUR Report I.01.113, JRC Ispra.

Casadei, F., May 2002. A hierarchic pinball method for contact-impact in fast transient dynamics. In: VI Congresso Nazionale della Società Italiana di Matematica Applicata e Industriale. Chia, Cagliari (Italy).

Casadei, F., December 2003a. A general impact-contact algorithm based on hierarchic pinballs for the europlexus software system. EUR Report I.03.176, JRC Ispra.

Casadei, F., November 2003b. Improvements in the module for inverse isoparametric mappings in europlexus. EUR Report I.03.132, JRC Ispra.

Casadei, F., Larcher, M., Valsamos, G., Faucher, V., September 2014a. Implementation of assembled surface normals and of a penalty contact formulation in the pinball model of europlexus. EUR Report EUR 26714 EN, JRC Ispra.

Casadei, F., Larcher, M., Valsamos, G., Langrand, B., avril 2014b. Pinball-based contact-impact model with parabolic elements in europlexus. EUR Report EUR 26629 EN (ISBN - JRC89913), JRC Ispra.

Caty, O., Maire, E., Youssef, S., Bouchet, R., 2008. Modeling the properties of closed-cell cellular materials from tomography images using finite shell elements. Acta Materialia 56 (19), 5524–5534.

Davoine, C., Portemont, G., Horezan, H., Langrand, B., Marcadon, V., Popoff, F., June 11-13 2014. Cellular materials made of stacked tubes: influence of the manufacturing process on the dynamic behavior of the constitutive material. Part I: microstructure. In: 14th ONERA-DLR Aerospace Symposium. Köln (Germany).

Dillard, T., Forest, S., Ienny, P., 2006. Micromorphic continuum modelling of the deformation and fracture behaviour of nickel foams. European Journal of Mechanics-A/Solids 25 (3), 526–549.

Evans, A. G., Hutchinson, J. W., Ashby, M. F., 1998. Multifunctionality of cellular metal systems. Progress in Materials Science 43 (3), 171–221.

Fallet, A., Lhuissier, P., Salvo, L., Bréchet, Y., 2008. Mechanical behaviour of metallic hollow spheres foam. Advanced Engineering Materials 10, 858–862.

Fazekas, A., Dendievel, R., Salvo, L., Bréchet, Y., 2002. Effect of microstructural topology upon the stiffness and strength of 2d cellular structures. International Journal of Mechanical Sciences 44 (10), 2047–2066.

Fiedler, T., Öchsner, A., 2008. On the anisotropy of adhesively bonded metallic hollow sphere structures. Scripta Materialia 58, 695–698.

Fiedler, T., Öchsner, A., Grácio, J., 2010. Numerical investigations on the mechanical properties of adhesively bonded hollow sphere structures. Journal of Composite Materials 44 (10), 1165–1178.

Florence, C., Sab, K., 2006. A rigorous homogenization method for the determination of the overall ultimate strength of periodic discrete media and an application to general hexagonal lattices of beams. European Journal of Mechanics-A/Solids 25 (1), 72–97.

Friedl, O., Motz, C., Peterlik, H., Puchegger, S., Reger, N., Pippan, R., 2008. Experimental investigation of mechanical properties of metallic hollow sphere structures. Metallurgical and Materials Transactions B 39, 135–146.

Gaitanaros, S., Kyriakides, S., Kraynik, A. M., 2012. On the crushing response of random open-cell foams. International Journal of Solids and Structures 49 (19–20), 2733 – 2743.

Gibson, L. J., Ashby, M. F., 1982. The mechanics of three-dimensional cellular materials. Proceedings of the Royal Society of London. Series A, Mathematical and Physical Sciences 382 (1782), 43–59.

Gibson, L. J., Ashby, M. F., 1997. Cellular solids: structure and properties, 2nd Edition. Cambridge University Press.

Gong, L., Kyriakides, S., 2005. Compressive response of open cell foams. Part II: Initiation and evolution of crushing. International Journal of Solids and Structures 42 (5–6), 1381 – 1399.

Gong, L., Kyriakides, S., Jang, W.-Y., 2005a. Compressive response of open-cell foams. Part I: Morphology and elastic properties. International Journal of Solids and Structures 42 (5–6), 1355 – 1379.

873 Gong, L., Kyriakides, S., Triantafyllidis, N., 2005b. On the stability of kelvin
874 cell foams under compressive loads. Journal of the Mechanics and Physics
875 of Solids 53 (4), 771 – 794.

876 Hallquist, J., Goudreau, G., Benson, D., 1985. Slinding interfaces with
877 contact-impact in large-scale lagrangian computation. Computer Methods
878 in Applied Mechanics and Engineering 51, 107–137.

879 Harders, H., Hupfer, K., Rösler, J., 2005. Influence of cell wall shape and
880 density on the mechanical behaviour of 2d foam structures. Acta materialia
881 53 (5), 1335–1345.

882 Hayes, A. M., Wang, A., Dempsey, B. M., McDowell, D. L., 2004. Mechanics
883 of linear cellular alloys. Mechanics of Materials 36 (8), 691–713.

884 Hönig, A., Stronge, W. J., 2002. In-plane dynamic crushing of honeycomb.
885 part i: crush band initiation and wave trapping. International Journal of
886 Mechanical Sciences 44 (8), 1665–1696.

887 Iltchev, A., Marcadon, V., Kruch, S., Forest, S., 2015. Computational ho-
888 mogenisation of periodic cellular materials: Application to structural mod-
889 elling. International Journal of Mechanical Sciences 93, 240 – 255.

890 Jang, W.-Y., Kraynik, A. M., Kyriakides, S., 2008. On the microstructure of
891 open-cell foams and its effect on elastic properties. International Journal
892 of Solids and Structures 45 (7–8), 1845 – 1875.

893 Jang, W.-Y., Kyriakides, S., Kraynik, A. M., 2010. On the compressive
894 strength of open-cell metal foams with kelvin and random cell structures.
895 International Journal of Solids and Structures 47 (21), 2872 – 2883.

896 Karagiozova, D., Yu, T., Gao, Z., 2006. Modelling of mhs cellular solid in
897 large strains. International Journal of Mechanical Sciences 48, 1273–1286.

898 Karagiozova, D., Yu, T. X., Gao, Z. Y., 2007. Stress-strain relationship for
899 metal hollow sphere materials as a function of their relative density. Journal
900 of Applied Mechanics 74, 898–907.

901 Lhuissier, P., Fallet, A., Salvo, L., Bréchet, Y., 2009. Quasistatic mechanical
902 behaviour of stainless steel hollow sphere foam: Macroscopic properties
903 and damage mechanisms followed by x-ray tomography. Materials Letters
904 63 (13), 1113–1116.

Mangipudi, K. R., Onck, P. R., 2011. Multiscale modelling of damage and failure in two-dimensional metallic foams. Journal of the Mechanics and Physics of Solids 59, 1437–1461.

Marcadon, V., Davoine, C., Passilly, B., Boivin, D., Popoff, F., Rafray, A., Kruch, S., 2012. Mechanical behaviour of hollow-tube stackings: Experimental characterization and modelling of the role of their constitutive material behaviour. Acta Materialia 60 (15), 5626–5644.

Marcadon, V., Feyel, F., 2009. Modelling of the compression behaviour of metallic hollow-sphere structures: About the influence of their architecture and their constitutive material's equations. Computational Materials Science 47 (2), 599–610.

Marcadon, V., Kruch, S., 2011. Roles of mechanical heterogeneities and damage on the overall mechanical behaviour of hollow-tube stackings. Procedia Engineering 10, 2815–2820.

Marcadon, V., Kruch, S., 2013. Influence of geometrical defects on the mechanical behaviour of hollow-sphere structures. International Journal of Solids and Structures 50, 498–510.

Ostoja-Starzewski, M., 2006. Material spatial randomness: From statistical to representative volume element. Probabilistic Engineering Mechanics 21 (2), 112–132.

Papka, S. D., Kyriakides, S., 1998. In-plane crushing of a polycarbonate honeycomb. International Journal of Solids and Structuress 35, 239–267.

Papka, S. D., Kyriakides, S., 1999a. Biaxial crushing of honeycombs. Part I: Experiments. International Journal of Solids and Structures 36 (29), 4367–4396.

Papka, S. D., Kyriakides, S., 1999b. In-plane biaxial crushing of honeycombs. Part II: Analysis. International Journal of Solids and Structures 36 (29), 4397–4423.

Portemont, G., Davoine, C., Langrand, B., Marcadon, V., June 11-13 2014. Cellular materials made of stacked tubes: influence of the manufacturing process on the dynamic behaviour of the constitutive material. Part

II: mechanical behaviour. In: 14th ONERA-DLR Aerospace Symposium. Köln (Germany).

Sanders, W. S., Gibson, L. J., 2003a. Mechanics of bcc and fcc hollow-sphere foams. Materials Science and Engineering: A 352 (1), 150–161.

Sanders, W. S., Gibson, L. J., 2003b. Mechanics of hollow sphere foams. Materials Science and Engineering: A 347 (1), 70–85.

Shim, V. P. W., Stronge, W. J., 1986. Lateral crushing of tightly packed arrays of thin-walled tubes. International Journal of Mechanical Sciences 28, 709–728.

Silva, M. J., Gibson, L. J., 1997. The effects of non-periodic microstructure and defects on the compressive strength of two-dimensional cellular solids. International Journal of Mechanical Sciences 39 (5), 549–563.

Silva, M. J., Hayes, W. C., Gibson, L. J., 1995. The effects of non-periodic microstructure on the elastic properties of two-dimensional cellular solids. International Journal of Mechanical Sciences 37 (11), 1161–1177.